colloids and interfaces

MDPI

Article

Thermodynamic Phase Control of Poly(TFEMA) Nucleation and Surface Deposition in Supercritical CO_2–Toluene

James R. Zelaya and Gary C. Tepper *

Department of Mechanical and Nuclear Engineering, Virginia Commonwealth University (VCU), Richmond, VA 23284, USA; zelayacanajr@vcu.edu

* Correspondence: gctepper@vcu.edu; Tel.: +1-804-827-4079

Abstract

The aim of this study was to investigate the nucleation, growth, and surface deposition of poly(2,2,2-trifluoroethyl methacrylate) [poly(TFEMA)] from the one-phase, cloud point, and two-phase regions of a supercritical CO_2–toluene solvent. A ternary mixture of 20 wt% toluene + 79 wt% $scCO_2$ + 1 wt% poly(TFEMA) at 40.0 °C was exposed to a fluorine-doped tin oxide (FTO) surface for 30 min at pressures placing the solution in (i) a one-phase region (15.86 MPa), (ii) the cloud point (12.37 MPa), and (iii) a two-phase region (8.96 MPa). Using the Altunin–Gadetskii–Haar–Gallagher–Kell (AG–HGK) equation of state (EOS), the corresponding CO_2 densities are 793.9, 729.2, and 477.8 kg m^{-3}. Scanning electron microscopy (SEM) and particle-size analysis (sample sizes N = 852–1177) show particle-size distributions (PSDs) that are well described by the following log-normal form: the mean diameter increases monotonically with a decrease in pressure (1.767 μm → 2.605 μm → 2.863 μm), while dispersion tightens slightly near the cloud point (coefficient of variation, CV: ≈0.47 → 0.44) and then broadens strongly in the two-phase region (CV ≈ 1.02). Morphologies transition from sparse, compact islands (one-phase) to agglomerated, necked spheres (cloud point) and finally hierarchical populations containing hollow/pitted large particles (two-phase). These outcomes are consistent with a phase-state-controlled shift in nucleation pathways, as follows: from heterogeneous surface nucleation in the one-phase regime to homogeneous nucleation with agglomeration at the cloud point, and to homogeneous nucleation with coalescence and solvent capture in the two-phase regime. The results provide a mechanistic basis and practical design rules for pressure-programmable control of fluoropolymer coatings prepared from $scCO_2$/aromatic-cosolvent systems.

Keywords: supercritical carbon dioxide ($scCO_2$); aromatic cosolvent; fluorinated methacrylate cloud point; homogeneous nucleation; heterogeneous nucleation; coalescence; particle-size distribution; fluoropolymer coatings; fluorine-doped tin oxide (FTO)

check for updates

Academic Editor: Volodymyr I. Kovalchuk

Received: 24 October 2025
Revised: 19 November 2025
Accepted: 20 November 2025
Published: 25 November 2025

Citation: Zelaya, J.R.; Tepper, G.C. Thermodynamic Phase Control of Poly(TFEMA) Nucleation and Surface Deposition in Supercritical CO_2–Toluene. *Colloids Interfaces* **2025**, *9*, 78. https://doi.org/10.3390/colloids9060078

Copyright: © 2025 by the authors. Licensee MDPI, Basel, Switzerland. This article is an open access article distributed under the terms and conditions of the Creative Commons Attribution (CC BY) license (https://creativecommons.org/licenses/by/4.0/).

1. Introduction

Controlling polymer nucleation pathways and the resulting particle and film morphologies is central to applications spanning superhydrophobic (anti-wetting) and antifouling coatings [1–3], optical control of haze and clarity [4], membranes [5–7], and particle-based functional interfaces [8]. Above the critical pressure and temperature of a solvent, the phase boundary between the liquid and vapor regions disappears. If a solute such as a polymer is present, the cloud point represents the temperature and pressure at which a second phase appears, often resulting in turbidity (cloudiness) due to light scattering from

nucleated particles. Therefore, a supercritical fluid solvent can be used to adjust solute nucleation by temperature and pressure control across the cloud point. $scCO_2$ is an attractive medium for such control because it combines liquid-like density with gas-like diffusivity, low viscosity, and nearly zero surface tension [9–12], properties that can be tuned by modest changes in pressure, temperature, or entrainer content to modulate supersaturation, nucleation barriers, and thus particle and film morphology [13–15]. These attributes, together with closed-loop recovery and residue-free venting, reduce volatile organic compound (VOC) emissions and align with green-chemistry principles [16,17]. In both industrial and academic settings, $scCO_2$ has enabled extraction [18–22], impregnation [23,24], templated porosity [25], microcellular foams [26], polymer synthesis [27], thin-film deposition [28–32], thin-film processing [33–35], and nanomaterials synthesis—from oxide nanoparticles [36,37] and energy materials [38] to exfoliated layered materials [39,40]. Despite these advantages, neat $scCO_2$ is a relatively weak solvent for polar solutes, and many polymers dissolve only sparingly without formulation aids [9,41].

A well-chosen organic cosolvent can broaden the solvency window of $scCO_2$ by strengthening solvent–solute interactions, shifting cloud points, and tuning interfacial properties, while preserving recyclability and residue-free venting [42–48]. Consistent with this, molecular dynamics studies show that nonpolar entrainers (e.g., toluene and cyclohexane) promote polymer dispersion in $scCO_2$, whereas strongly hydrogen-bonding cosolvents underperform due to self-association [49]. Among aromatics, toluene is especially practical; it enhances the solubility of methacrylic species and remains compatible with $scCO_2$-rich phases across accessible processing conditions [50,51]. The $scCO_2$–toluene system is underpinned by extensive thermophysical data, that is, pressure–density–temperature relations, vapor–liquid equilibria, critical loci, and accurate equations of state, which allow the precise placement of operating points near the critical region [50–54]. As shown in Figure 1, toluene is an aprotic aromatic; its delocalized π system strengthens dispersive interactions with ester carbonyls without promoting strong hydrogen-bond networks, consistent with reports that hydrogen-bonding entrainers (e.g., methanol) restructure solvation in modified $scCO_2$ [46] and that specific cosolvent–solute interactions drive the largest solvency gains in supercritical fluids [42], thereby broadening $scCO_2$ solvency while allowing facile cosolvent removal upon venting.

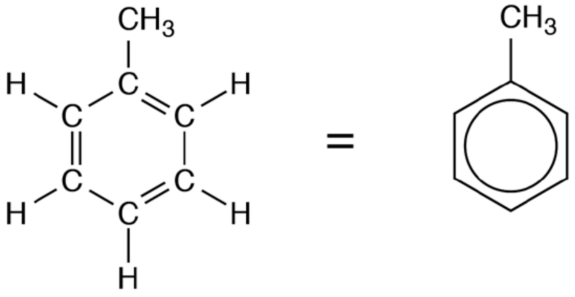

Figure 1. Toluene depictions: expanded Kekulé form (**left**) and aromatic shorthand indicating a delocalized π system (**right**). Aprotic and π-polarizable, toluene is compatible with $scCO_2$-rich phases and broadens the solvency window, shifting cloud points.

Fluoropolymers have widespread use in coatings and films due to their low-surface-energy hydrophobicity, outstanding chemical and corrosion resistance, UV and weathering durability, thermal stability, and excellent dielectric insulation [55–57]. They can exhibit significant solubility in dense $scCO_2$ under the appropriate temperature–pressure conditions [41,43]. Within this class, poly(TFEMA) is an appealing target for supercritical processing. As highlighted in Figure 2, the repeat unit presents an ester carbonyl (C=O) and a terminal CF_3 on a 2,2,2-trifluoroethyl pendant—CO_2-philic motifs associated with

enhanced compatibility in $scCO_2$-rich media [58]. Elevated $scCO_2$ activity further plasticizes the methacrylate backbone, effectively depressing T_g and increasing chain mobility during growth and coalescence [59]. In our recent cloud-point study at 31.5–50.0 °C, adding toluene monotonically reduced the dissolution pressure of poly(TFEMA) by up to about 40% at 20 wt% entrainer, thereby expanding practical processing windows for deposition and particle formation [60]. Consistent with broader trends, fluorinated (meth)acrylate copolymers exhibit solvent-dependent critical-solution behavior and molecular-weight-sensitive cloud points in supercritical fluorinated solvents [61]. Poly(TFEMA) has been precipitated as nano- and microparticles and as hydrophobic coatings from supercritical solutions without persistent solvent burdens [8,62]. Previous work from our group demonstrated $scCO_2$-enabled perovskite crystallization and the incorporation of polymers into perovskite films at low temperature, connecting phase-controlled processing to improved functional performance [23,63–66].

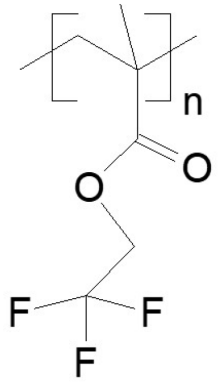

Figure 2. Repeat unit of poly(TFEMA): a methacrylate backbone bearing a 2,2,2-trifluoroethyl ester pendant. The carbonyl (C=O) and terminal CF_3 groups are CO_2-philic motifs associated with compatibility in $scCO_2$-rich phases.

The thermodynamic phase state of the processing medium governs the route from dissolved solute to precipitated particles and films [67–69]. Classical nucleation theory indicates that, in dilute single-phase solutions with favorable solvent–solute interactions, homogeneous nucleation rates are vanishingly small because the free-energy barrier is high [68,69]. Crossing a phase boundary into a two-phase region increases supersaturation and lowers this barrier so that bulk (homogeneous) nucleation becomes competitive [69,70]. At all states, pre-existing surfaces reduce the barrier and often dominate the kinetics, so heterogeneous nucleation can operate in both single- and two-phase regimes [70–72]. Once nuclei form, growth and coarsening reflect the prevailing transport as follows: under diffusion-controlled ripening, the system evolves toward a self-similar size distribution with a sharp upper cutoff and a mean radius that increases characteristically with time [73]. During the depressurization of a supercritical-fluid solvent, solvent pockets trapped within the polymer phase can outgas, leaving pits or hollows typical of gas-blown polymers [3,5,7]. This framework provides a direct mapping from thermodynamic state to nucleation pathway and, ultimately, to the particle-size and morphology observables we measure.

Although $scCO_2$ processing of fluorinated (meth)acrylates is well documented, the relationship between thermodynamic phase and particle nucleation and surface deposition remains underdeveloped. Here, we hold composition and temperature constant (40.0 °C) and vary only pressure to traverse the one-phase, cloud-point, and two-phase regimes in a $scCO_2$–toluene–poly(TFEMA) system. Pressures were selected from our cloud-point measurements to ensure reproducible placement in each regime [60]. We show that the phase state deterministically selects the dominant nucleation pathway—heterogeneous

surface nucleation in the one-phase regime; homogeneous nucleation with agglomeration at the cloud point; and accelerated homogeneous nucleation with coalescence in the two-phase regime—driving a systematic shift in particle size, dispersion, and morphology.

These results establish some processing guidelines for tuning fluoropolymer particle size, dispersion, and porosity in $scCO_2$ with aromatic cosolvents, thereby providing practical design rules for coatings and particle fabrication.

2. Materials and Methods

2.1. Materials

- Carbon dioxide (CO_2), obtained from Airgas (Philadelphia, PA, USA); certified purity 99.9995%.
- Poly(2,2,2-trifluoroethyl methacrylate) [poly(TFEMA); trifluoroethyl methacrylate homopolymer], obtained from Specific Polymers (Castries, France). Supplier data: $M_n = 31{,}283\ \mathrm{g\,mol^{-1}}$, $M_w = 65{,}501\ \mathrm{g\,mol^{-1}}$, and PDI = 2.1.
- Toluene (C_7H_8; 99.8%), obtained from Sigma-Aldrich (St. Louis, MO, USA).
- Fluorine-doped tin oxide (FTO) coated glass substrates, 25 mm × 25 mm, obtained from Ossila Ltd. (Solpro Business Park, Windsor Street, Sheffield, S4 7WB, UK).

Unless otherwise stated, all materials were used as received without further purification.

2.2. Substrate Preparation

Fluorine-doped tin oxide (FTO) substrates were cleaned using a multistep protocol to remove organic and particulate contaminants, improve wettability, and ensure reproducible polymer deposition. The procedure was as follows:

1. Initial wash: Substrates were washed with a solution of deionized (DI) water and Alconox detergent (Powder Precision Cleaner, Sigma-Aldrich), and they were then rinsed with DI water and placed into a polypropylene substrate cleaning rack (Ossila, Product Code E102).
2. Ultrasonic cleaning with Hellmanex: The rack was placed in a Branson Ultrasonic Cleaner (Model 1510; Branson Ultrasonics Corp., Wallingford, CT, USA). A Hellmanex III working solution (prepared by diluting 2 mL Hellmanex III, Ossila, in 100 mL DI water) was added to the rack compartments. The ultrasonic bath reservoir was filled with water to a level just below the top of the rack height to ensure full immersion. Sonication was performed for 15 min at ambient temperature.
3. Rinsing: Substrates were removed and rinsed with DI water to remove Hellmanex residues.
4. Sequential solvent sonication: Substrates were sonicated first in isopropyl alcohol (IPA, ≥99.7%, Sigma-Aldrich) for 15 min, followed by acetone (≥99.5%, Sigma-Aldrich) for 15 min.
5. Final rinses and drying: After solvent sonication, substrates were rinsed with acetone and then with IPA, and they were quickly dried using a stream of high-pressure dry air to prevent residues or liquid spots.
6. Plasma treatment: Substrates were plasma-cleaned for 4 min in a Solarus 950 advanced plasma system (Gatan Inc., Pleasanton, CA, USA). The plasma environment consisted of 75% argon and 25% oxygen at 25 psi, with feed gases of 99.995% purity.

This protocol effectively removed surface contaminants and produced a hydrophilic, high-energy surface favorable for polymer nucleation and adhesion during subsequent supercritical deposition.

2.3. Supercritical Deposition System and Instrumentation

Figure 3 is a schematic illustration of the experimental system used to deposit poly(TFEMA) onto FTO substrates from $scCO_2$ with cosolvent at well-defined pressure–temperature conditions. The system includes components for CO_2 delivery and pressurization, a high-pressure Parr deposition chamber, external heating with in situ monitoring, and a video/data acquisition chain. The primary components are the following:

1. CO_2 cylinder: High-purity CO_2 was supplied from a compressed-gas cylinder via high-pressure stainless-steel tubing and a control valve to the syringe pump, providing a clean and continuous feed.
2. Syringe pump: Teledyne ISCO 260D (Teledyne Isco, Lincoln, NE, USA) pressurized and delivered CO_2 to the pressure vessel with precise control of delivery rate and final set pressure, enabling reproducible attainment of the one-phase, cloud-point, and two-phase conditions.
3. Pump-head chiller: Neslab CFT-25 refrigerated recirculator (Neslab Instruments Inc., Portsmouth, NH, USA) cooled the syringe pump head to increase CO_2 density during each loading cycle, thereby increasing the mass delivered per stroke and reducing the number of charging iterations needed to reach the target vessel pressure.
4. High-pressure vessel: Parr 4768 reactor (Parr Instrument Company, Moline, IL, USA) housed the substrates, polymer, cosolvent, and $scCO_2$ during deposition (nominal capacity 600 mL). The effective working volume was experimentally determined by an Archimedes displacement procedure to be 424.89 mL, with an estimated uncertainty of ±3 mL. Key specifications: head style VGR; maximum working pressure 3000 psi at 350 °C; and maximum working temperature 350 °C with flat PTFE gasket.
5. Heating and temperature monitoring: A Staco Variac autotransformer (Model 3PN1010B; Staco Energy Products Co., Dayton, OH, USA; input 120 V, output 0–140 V, 12 A, 1.4 kVA) powered a heavy-duty heating tape (HTS/Amptek AWD-051-060, Stafford, TX, USA; 120 V, 312 W) wrapped around the vessel to regulate temperature. The internal temperature was measured with a J-type thermocouple inserted through the head of the vessel (the rod extending into the chamber) and read on an OMEGA HH506 digital thermometer (Omega Engineering Inc., Norwalk, CT, USA; 0.1 °C readout resolution). All deposition experiments were carried out at a nominal set point of 40.0 °C, with the vessel temperature stable within approximately ± 0.2 during the 30 min hold. This set point was then converted to 313.2 K for use where an absolute temperature is required.
6. Pressure monitoring: The vessel pressure was measured using an OMEGA PX309-10KGI pressure transducer with readout on an OMEGA DP400TP high-speed panel meter (Omega Engineering Inc., Norwalk, CT, USA). The combined system precision was $\pm 0.25\%$ of full scale (including linearity, hysteresis, and repeatability), providing reliable real-time control. Pressures were read in psi and converted to MPa for reporting; on the 10,000 psi range, this specification corresponds to an absolute uncertainty of approximately ± 0.17 MPa. Throughout this work, tabulated pressures in MPa should therefore be regarded as nominal set points with this uncertainty, unless a different value is stated explicitly.
7. Video monitoring: A Vanxse CCTV Mini HD 1/3 CCD 960H Auto Iris Camera (Model BX2812; Shenzhen Kaixing Security Technology Co., Ltd., Shenzhen, China; NTSC) recorded the HH506 (temperature) and DP400TP (pressure) displays. The signal passed through a NOVPEAK BNC CCTV S-Video to VGA converter (Model UPD39 E01A; SQdeal) and an ATCCPYDM VGA-to-USB 2.0 capture card (Model V2U-LO) prior to transfer to the computer.

8. Data acquisition: Video files containing synchronized pressure and temperature readings were captured and archived for each run using OBS Studio 30.0.2 (OBS Project, open-source). These time-stamped recordings were used for post hoc frame-by-frame analysis to verify vessel conditions and improve the accuracy of the reported experimental values across all deposition regimes.

Collectively, the system allows for the control of pressure–temperature trajectories to access the one-phase, cloud-point, and two-phase states at 40.0 °C. The effective volume of the pressure vessel determined experimentally, combined with equation-of-state CO_2 densities [54], enabled quantitative mass balances for $scCO_2$ loading. The ISCO 260D with pump-head chilling reduced charging iterations and improved run-to-run repeatability; the Variac/tape-heater with thermocouple feedback maintained stable isothermal deposition; and the PX309 transducer with DP400TP readout provided ±0.25% full-scale accuracy for reliable set-point control. Time-stamped recordings captured in OBS Studio 30.0.2 created a complete audit trail of temperature and pressure histories, underpinning the reproducibility and post hoc verification of all reported conditions.

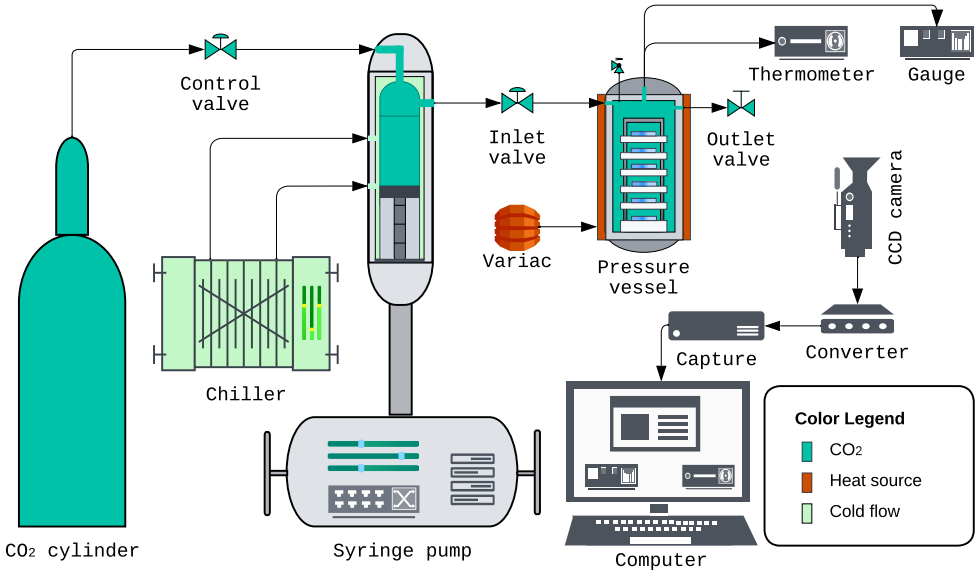

Figure 3. Schematic diagram illustrating the primary components used to study the deposition of poly(TFEMA) in $scCO_2$ with toluene cosolvent, operated at one-phase, cloud-point, and two-phase conditions.

2.4. Cloud-Point References and Set-Point Selection

Cloud-point information was used to establish the three deposition pressures (one-phase, cloud-point, and two-phase) at 40.0 °C (313.2 K). We chose 313.2 K to maintain continuity with our prior cloud-point study at the same temperature [60], which provides the reference trend used here. In the present experiments, the toluene content remained at 20 wt%, while the polymer fraction was reduced from 3 to 1 wt% (the balance being an increase in CO_2). Because toluene strengthens CO_2 solvency for poly(TFEMA), we expect the cloud point to be less sensitive to small changes in polymer fraction in the ternary solution compared to neat CO_2. Therefore, the potential change in the cloud point in the ternary solution as the polymer concentration is reduced from 3 wt% to 1 wt% was estimated from independent neat-CO_2 measurements.

Cloud points were measured for poly(TFEMA) in neat CO_2 at 2, 3, and 5 wt% over 304.7–323.2 K (31.5–50.0 °C). These neat-CO_2 data were used to determine the sensitivity to

polymer fraction at 313.2 K and thus define the uncertainty range when moving from 3 to 1 wt% polymer at fixed 20 wt% toluene. The full dataset is summarized in Table 1.

Table 1. Poly(TFEMA) cloud-point pressures in neat CO_2. Mean of ≥6 measurements per entry (repeatability is within ±1% of the reported value). The bolded 313.2 K row is used to estimate the polymer–fraction sensitivity at the deposition temperature.

Temperature (K)	Cloud Point Pressure (MPa)		
	2 wt% Poly(TFEMA)	3 wt% Poly(TFEMA) [a]	5 wt% Poly(TFEMA)
304.7	18.35	18.52	19.17
308.2	20.78	20.84	20.87
313.2	**23.05**	**23.32**	**23.46**
318.2	24.97	25.38	25.85
323.2	27.01	27.37	27.92

[a] 3 wt% values from our previous publication [60].

Cloud points for Table 1 were obtained with a variable-volume phase monitor (30 mL quartz-window syringe-pump cell; Supercritical Fluid Technologies, Inc., Newark, DE, USA; SFT) using the reversible-turbidity criterion, outlined as follows: stepwise decompression from a verified one-phase state to the first persistent haze by CCD imaging, followed by re-compression to recover clarity. Each entry is the mean of at least six independent determinations at fixed composition and temperature.

Using the 313.2 K row in Table 1, the local dependence of cloud-point pressure on polymer mass fraction in neat CO_2 is estimated by a secant finite difference between 2 and 5 wt%:

$$\left.\frac{\partial P_{cp}}{\partial w_p}\right|_{313.2\ \mathrm{K}} \approx \frac{23.46 - 23.05}{5 - 2} = 0.137\ \mathrm{MPa\,wt\%^{-1}}.$$

Consequently, reducing the polymer from 3 to 1 wt% is expected to lower P_{cp} by ≈0.274 MPa (about 1.17%). To transfer the 3 wt% reference to 1 wt% in the ternary solution, we define a composition-transfer envelope equal to the full spread of the neat-CO_2 values at 313.2 K across 2–5 wt% about the 3 wt% point ($\Delta w_p = 3$ wt%) as follows: ±1.76% (that is, $(23.46 - 23.05)/23.32 \times 100\%$). This envelope intentionally exceeds the actual 2 wt% decrement used here and therefore builds in a safety margin.

Figure 4 complements Table 1 by showing the near-linear increase of P_{cp} with temperature in neat CO_2 and the modest upward shift with increasing polymer fraction; the absolute spread at 313.2 K is only 0.41 MPa (23.46–23.05 MPa), consistent with the adopted envelope.

To obtain a single working band for set-point choice, we combine (i) the ±1.76% composition-transfer envelope with (ii) the cloud-point measurement repeatability, ±1.0% (based on ≥6 cycles per point). Treating these as independent contributions and combining by root-sum-of-squares yields an overall relative uncertainty of ±2.02%. Applying this to the 12.37 MPa reference at 313.2 K gives a cloud band of 12.12–12.62 MPa for the mixture with 20 wt% toluene + 1 wt% poly(TFEMA) + 79 wt% CO_2. Operationally, we interpret any isobar that lies within this band as "at the cloud point" for the 1 wt% polymer ternary; isobars that lie well above or below the band are assigned to the one-phase or two-phase fields, respectively. The band and the three isothermal deposition pressures are summarized in Figure 5.

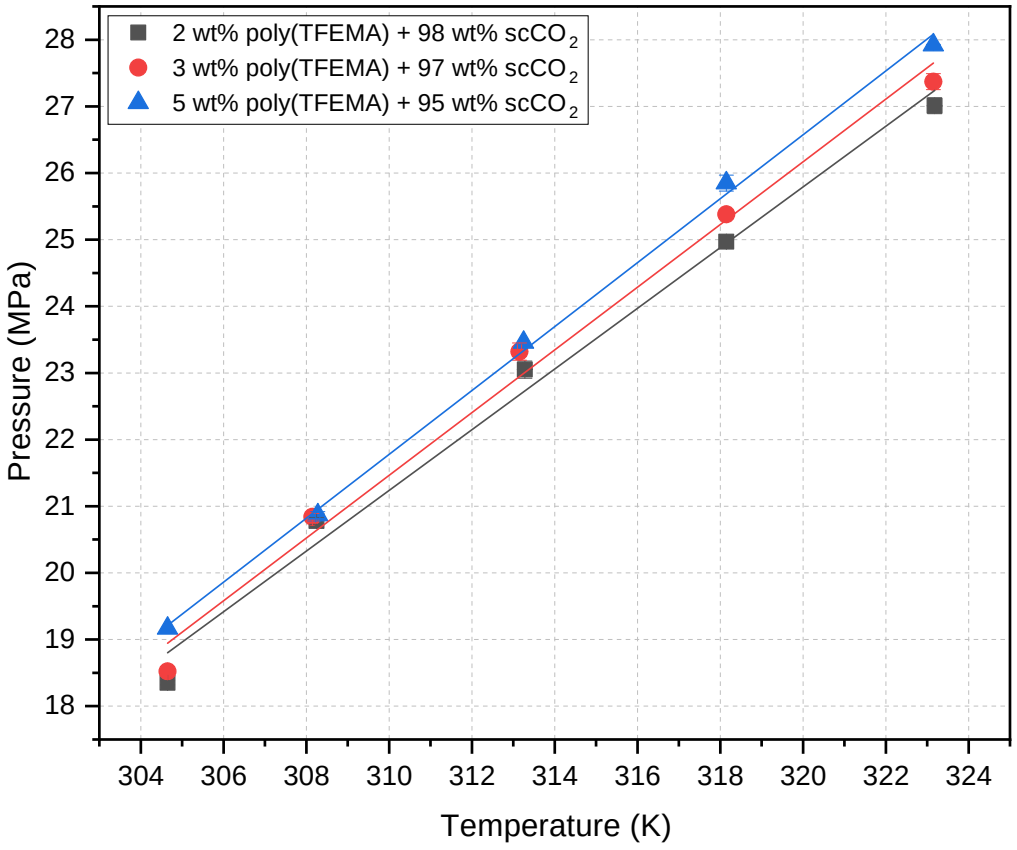

Figure 4. Cloud-point pressure vs. temperature for 2, 3, and 5 wt% poly(TFEMA) in $scCO_2$. Error bars are within ±1% of the reported value. The 3 wt% trend was reported in our previous publication and is reused here solely for comparison [60].

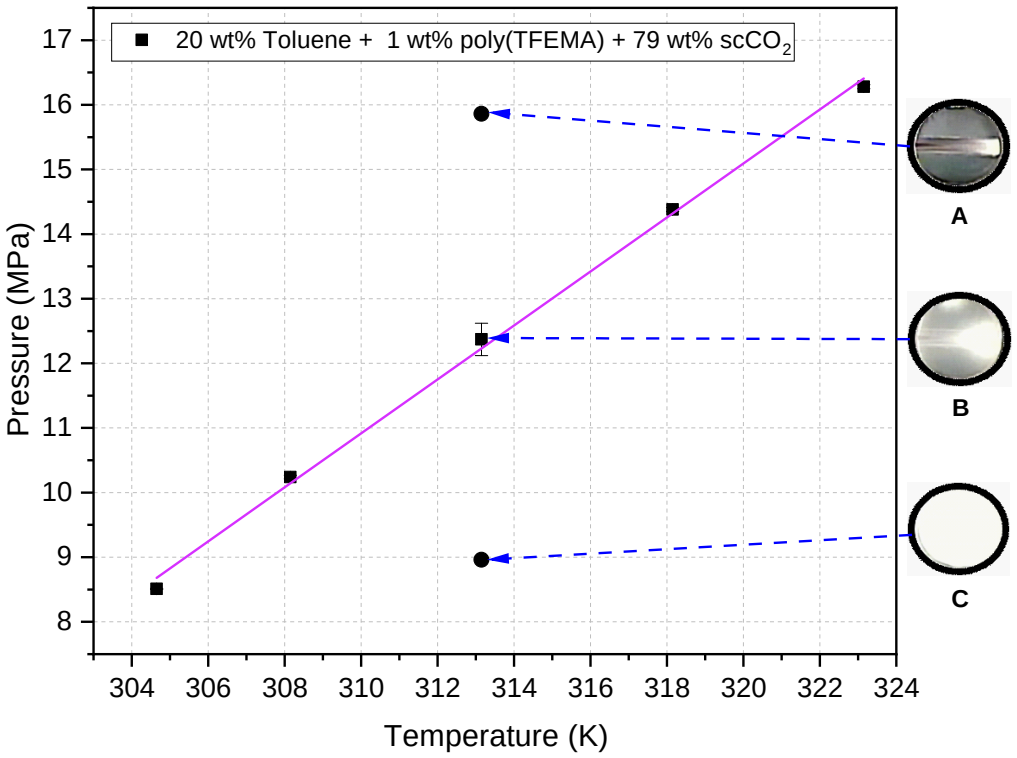

Figure 5. Cloud-point reference for 20 wt% toluene + 1 wt% poly(TFEMA) + 79 wt% CO_2 at 313.2 K. Error bars denote the ±2.02% working band. Phase-monitor images illustrate (**A**) one-phase, (**B**) cloud point, and (**C**) two-phase regions under the deposition conditions.

Figure 5 shows how the cloud-point reference was applied. The solid line and square symbols are carried over from the earlier 3 wt% polymer dataset [60]; in the present context, the vertical error bars on those points represent the conservative ±2.02% uncertainty range applied to the 1 wt% case. The dashed horizontal lines locate the three isobars used for deposition at 313.2 K. Their positions relative to the reference at 313.2 K identify the sampled phase fields: (A) at 15.86 MPa corresponds to the one-phase region, (B) at 12.37 MPa lies within the transfer band and is therefore taken as the cloud point, and (C) at 8.96 MPa falls in the two-phase region where turbidity persists. The accompanying CCD images (A–C) provide direct visual confirmation of these assignments, showing, respectively, a clear one-phase state, the onset of turbidity, and a fully phase-separated system.

Finally, depositions were performed at the three set points listed in Table 2, corresponding to one-phase, cloud-point, and two-phase operation, respectively. The one-phase and two-phase set points lie more than 3.1 MPa above and below the 12.12–12.62 MPa band, ensuring unambiguous phase-state assignment, while the cloud-point set point is intentionally centered within the band.

Table 2. Phase-state assignment at 313.2 K for 20 wt% toluene + 1 wt% poly(TFEMA) + 79 wt% CO_2.

Pressure (MPa)	Classification
15.86 ± 0.17	One-phase
12.37 ± 0.25	Cloud point
8.96 ± 0.17	Two-phase

2.5. Deposition Procedures and Compositions

Deposition experiments were executed at the three isothermal pressures identified in Figure 5 for the mixture containing 20 wt% toluene + 1 wt% poly(TFEMA) + 79 wt% $scCO_2$ at 40.0 °C (313.2 K). As labeled in Figure 5, these are as follows: (A) 15.86 MPa in the one-phase region, (B) 12.37 MPa at the cloud point (first persistent haze), and (C) 8.96 MPa in the two-phase region. Panels A–C are CCD snapshots through the quartz window of the variable-volume phase monitor (30 mL syringe-pump cell; SFT) and illustrate the optical criteria used to confirm the targeted regime during each run.

Consistent with our prior protocol [60], the $scCO_2$ mass at each set point was calculated from the pure-CO_2 density, $\rho_{scCO_2}(T, P)$, using the Altunin–Gadetskii base EOS with the Haar–Gallagher–Kell near-critical correction (AG–HGK) for CO_2, following the formulation of Pitzer and Schreiber [54], at 313.2 K and the measured isothermal pressure for each condition; this density was then multiplied by the vessel's effective volume (424.89 mL). In doing so, we neglected mixture-density corrections and the small volume displaced by the charged toluene and polymer. Attempts to obtain m_{scCO_2} gravimetrically with an interposed transfer vessel were confounded by low ΔP, extended thermal equilibration, and cosolvent and polymer backflow; we therefore assign a conservative ±5% uncertainty to m_{scCO_2}. Toluene and polymer amounts were then set to maintain 20 wt% and 1 wt%, respectively. Poly(TFEMA) masses were weighed using an analytical balance (Accu-124, Fisher Scientific, Waltham, MA, USA; capacity 120 g, readability 0.1 mg, linearity ±0.2 mg), and toluene volumes were dispensed with calibrated pipettes, so the uncertainties in toluene and polymer amounts are negligible compared with the conservative ±5% relative uncertainty assigned to m_{scCO_2}. The resulting solute and solvent conditions for each phase region are summarized in Table 3.

Table 3. Charges and $scCO_2$ properties used for polymer deposition at 313.2 K (40.0 °C) for the mixture with 20 wt% toluene + 1 wt% poly(TFEMA) + 79 wt% $scCO_2$.

Regime	P (MPa)	ρ_{scCO_2} (kg m^{-3})	m_{scCO_2} (g)	m_{Tol} (g)	V_{Tol} (mL)	m_{Poly} (g)
One-phase	15.86	793.9	337.3	85.4	99.0	4.3
Cloud point	12.37	729.2	309.8	78.4	91.0	3.9
Two-phase	8.96	477.8	203.0	51.4	59.6	2.6

Pressures are nominal set points; their uncertainties are given in Table 2.

Common operating protocol (applies to all three conditions).

- Charge and fixturing. Dispense the prescribed toluene volume (Table 3) into the open vessel using a beaker and calibrated pipette. Mount one cleaned substrate on each of the top three rack levels; place the weighed poly(TFEMA) on the fourth level, directly beneath the lowest substrate.
- Sealing and heating. Install the head; tighten bolts in a star pattern in 5 lb-ft increments to a final torque of 25 lb-ft (∼34 N·m). Apply heat with a Variac-driven tape and equilibrate at 40.0 °C (313.2 K).
- CO_2 introduction and purge. With the syringe pump set to 20 mL min^{-1}, pressurize to ∼3.45 MPa (∼500 psi), then purge three times by venting to ∼2.07 MPa (∼300 psi) and repressurizing to remove air and moisture while retaining polymer and toluene (outlet valve cracked only minimally).
- Stabilization. Resume CO_2 addition and follow the pressure path specific to the targeted regime (as specified in Pressure paths and rationale, below). Start the 30 min deposition clock only when both temperature (313.2 K) and pressure are stable.

Pressure paths and rationale.

- One-phase, 15.86 MPa. Pressurize directly at 20 mL min^{-1} to 15.86 MPa at 313.2 K; close the inlet valve to isolate; hold 30 min. This sets a homogeneous one-phase state throughout the treatment, consistent with the clear-field phase-monitor image in Figure 5A.
- Cloud point, 12.37 MPa. First pressurize to ≈12.62 MPa at 313.2 K (one-phase region) to ensure complete dissolution; then reduce slowly to 12.37 MPa by cracking the outlet valve to minimize solvent or polymer loss; hold 30 min. The visual endpoint is the first persistent haze captured through the phase monitor (Figure 5B), our reversible-turbidity criterion.
- Two-phase, 8.96 MPa. First pressurize to ≈12.41 MPa at 313.2 K to dissolve polymer; then decompress slowly to 8.96 MPa; hold 30 min. The phase monitor shows sustained turbidity at this isobar (Figure 5C), confirming operation in the polymer-saturated two-phase region.

Post-treatment handling.

- Immerse the vessel in an ice–water bath (0.0 °C) while sealed to precipitate toluene from the supercritical phase and quench further mass transfer.
- When the external thermometer reads ∼16.0 °C, vent slowly and continuously to ambient pressure, remove the head, and retrieve the substrates for ex situ characterization.

The dashed lines and annotated images in Figure 5 therefore serve a dual role as follows: they document the optical criteria used to identify the one-phase, cloud-point, and two-phase regimes at 313.2 K, and they verify that the operational pressure paths above consistently place the system in those regimes during the 30 min deposition window.

2.6. SEM Preparation and Imaging

Prior to imaging, FTO substrates bearing poly(TFEMA) deposits were sputter-coated with gold using a Polaron Plasma Sputter Coating System (Quorum Technologies, Lewes, UK). The chamber was evacuated to ∼10 Pa, the discharge current stabilized at ∼10 mA, and sputtering proceeded for 60 s. SEM imaging was performed on a Hitachi SU-70 Ultra High-Resolution Analytical Field-Emission SEM (Hitachi High-Technologies, Tokyo, Japan; Schottky emitter) in secondary-electron mode at 5.0 kV.

3. Results and Discussion

3.1. Phase-State Control of Deposition (Overview)

Poly(TFEMA) deposits were obtained under the one-phase, cloud-point, and two-phase conditions defined in Section 2.5, using pressure to tune the CO_2 density and solvency at fixed composition and temperature.

The size distributions and morphology of the deposited particles at each phase state were measured and are consistent with lognormal statistics, typical of diffusion-limited, multiplicative growth in polymer precipitation. However, the mean size, dispersion, spatial organization, and surface morphology varied strongly with phase state. The data reveal a progression from heterogeneous surface-mediated nucleation with sparse, flattened surface islands (one-phase region), to the onset of homogeneous nucleation in solution with spherical particle agglomeration (cloud point), and finally to extensive coalescence with solvent capture and depressurization-induced gas-release features that yield pitted large particles (two-phase region). The cloud-point condition was established from independent phase-monitor measurements (Figure 5) and is described in detail in Section 2.4.

3.2. One-Phase Region

At 40.0 °C and 15.86 MPa, the ternary mixture resides in a one-phase state (Figure 5A). Under these conditions, poly(TFEMA) remains fully dissolved throughout the 30 min deposition period; homogeneous nucleation is, therefore, expected to be absent and particle formation is limited to heterogeneous surface nucleation. The representative SEM micrograph in Figure 6 exhibits the diagnostic hallmarks of this regime as follows: (i) a sparse, essentially monolayer coverage with center-to-center spacings of multiple diameters; (ii) near-circular polymer islands rather than spherical particles, indicating surface-mediated heterogeneous nucleation and lateral growth rather than homogeneous nucleation and growth in solution followed by deposition; and (iii) the absence of particle clusters or agglomerates. Taken together, this morphology is consistent with heterogeneous surface nucleation and growth.

Figure 7 shows the particle-size distribution (PSD) for deposition from the one-phase region. The histogram is unimodal with a pronounced peak at ∼1.30 µm and a gently decaying right tail extending to ∼4–5 µm. The arithmetic descriptors are $\mu = 1.767$ µm and $\sigma = 0.8367$ µm for $N = 1177$ particles (coefficient of variation CV ≈ 0.47), indicating a moderately narrow dispersion. Two qualitative features are diagnostic. First, the absence of a secondary peak or a low-diameter shoulder argues against homogeneous nucleation in solution. Second, the scarcity of very large particles shows that heterogeneous surface nucleation was initiated broadly and uniformly across the FTO surface. These statistical signatures mirror the morphology in Figure 6, where most particles fall between 1 and 2 µm and only occasionally approach the 3 µm scale bar. Sampling precision is high (standard error of the mean $\sigma/\sqrt{N} \approx 0.024$ µm; 95% CI $\mu \pm 0.048$ µm), supporting reliable cross-condition comparisons.

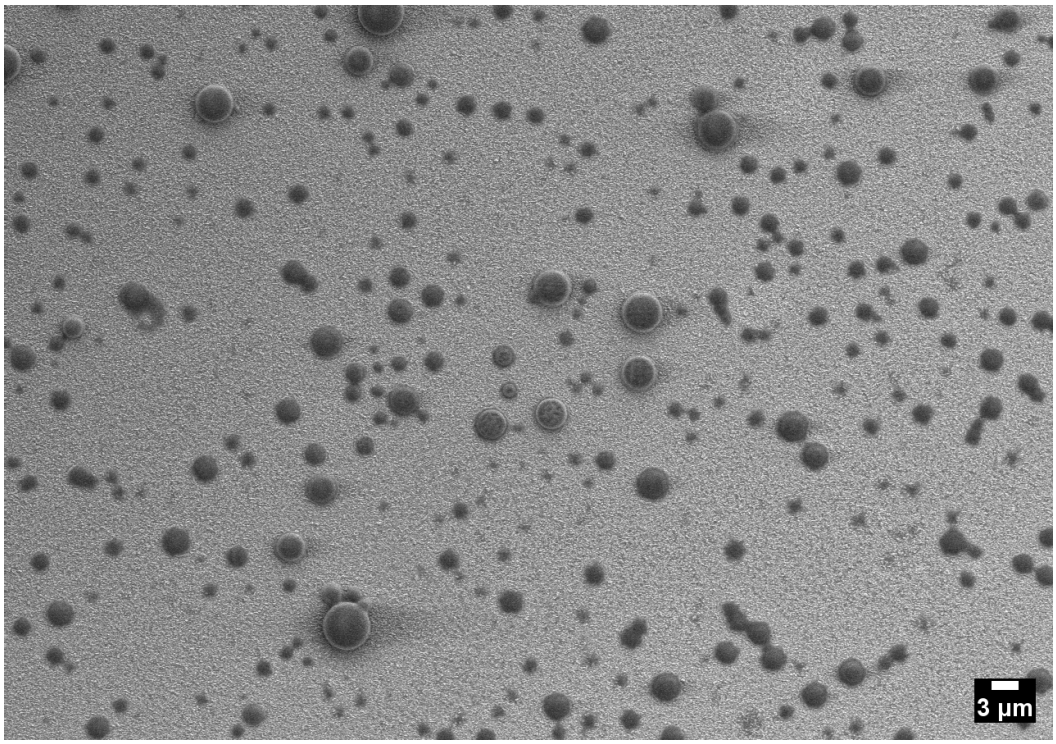

Figure 6. SEM image of the one-phase region (40.0 °C, 15.86 MPa) showing sparse, near-circular poly(TFEMA) islands on FTO with minimal necking.

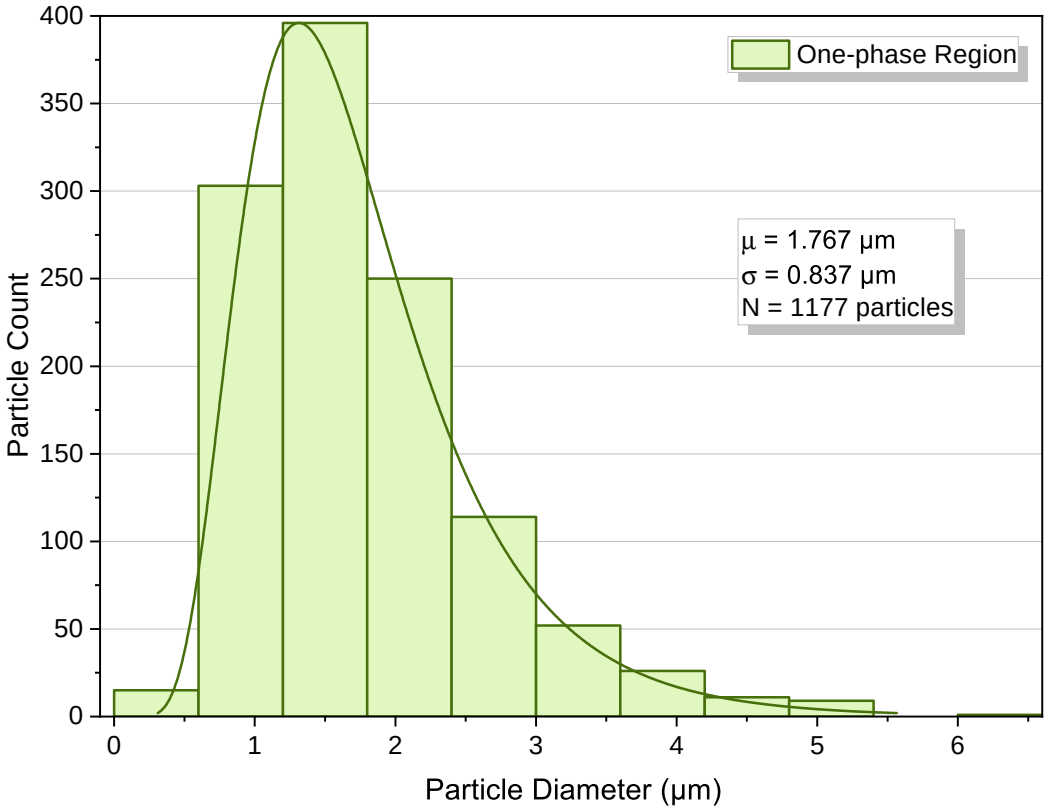

Figure 7. PSD in the one-phase region (40.0 °C, 15.86 MPa), following a lognormal distribution (solid green line): μ = 1.767 µm, σ = 0.837 µm, $N = 1177$, and CV $\approx$ 0.47; histogram mode $\sim$ 1.30 µm.

The physical origin of the observed deposition from the one-phase solution is consistent with heterogeneous, surface-mediated nucleation followed by diffusion-limited growth. During the 30 min deposition period, the polymer remains dissolved (high bulk

free-energy barrier), so nucleation can only occur at FTO surface sites. Once initiated, polymer islands grow laterally at the edges by diffusive supply from their local environment, giving rise to the familiar lognormal distribution with a short right tail.

As a whole, the SEM morphology and the PSD indicate surface-mediated nucleation and diffusion-limited growth yielding isolated, compact deposition sites with a relatively narrow size distribution. We adopt this one-phase deposition result as the baseline for the comparisons that follow, and next we examine how particle formation and surface deposition occur in the cloud-point and two-phase regions.

3.3. Cloud-Point Condition

At 40.0 °C and 12.37 MPa, the ternary mixture resides near the cloud point (Figure 5B). The cloud point was established optically using the phase monitor and is defined here as the first appearance of persistent haze. This turbidity reflects polymer-rich domains produced by bulk homogeneous nucleation, which scatter light and account for the visible haze, marking entry into the two-phase region. The SEM micrograph in Figure 8 shows ensembles of agglomerated spherical particles and a noticeable increase in particle number density and size compared to the one-phase region (Figure 6). The grape-like clusters of well-formed, spherical particles indicate solution nucleation and growth with agglomeration and limited coalescence.

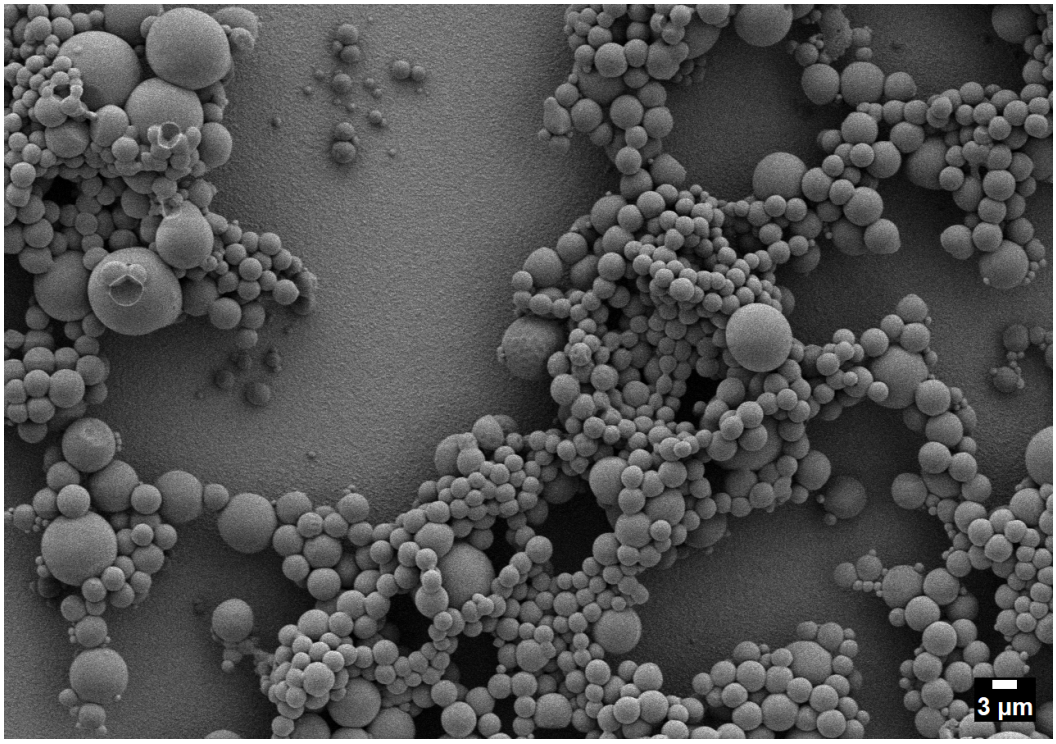

Figure 8. SEM image of the cloud-point condition (40.0 °C, 12.37 MPa) showing clustered spherical agglomerates of poly(TFEMA) on FTO.

Figure 9 is a histogram that illustrates the PSD. The data follow a lognormal distribution, consistent with multiplicative, diffusion-limited particle growth. The distribution is unimodal with a pronounced peak at ∼2.00 µm and a right tail extending to ∼7–10 µm. The arithmetic descriptors are $\mu = 2.605$ µm and $\sigma = 1.140$ µm for $N = 852$ (CV ≈ 0.44), indicating a broader, upward-shifted dispersion relative to the one-phase baseline ($\mu = 1.767$ µm; mode ∼1.30 µm). The absence of a low-diameter shoulder or a secondary peak argues against prolonged, multi-epoch nucleation, and the coexistence of necked contacts with a still-unimodal PSD indicates limited coalescence that forms bridges without erasing

particulate identity. Sampling precision is high (standard error $\sigma/\sqrt{N} \approx 0.039$ µm; 95% CI $\mu \pm 0.077$ µm), supporting reliable cross-condition comparisons.

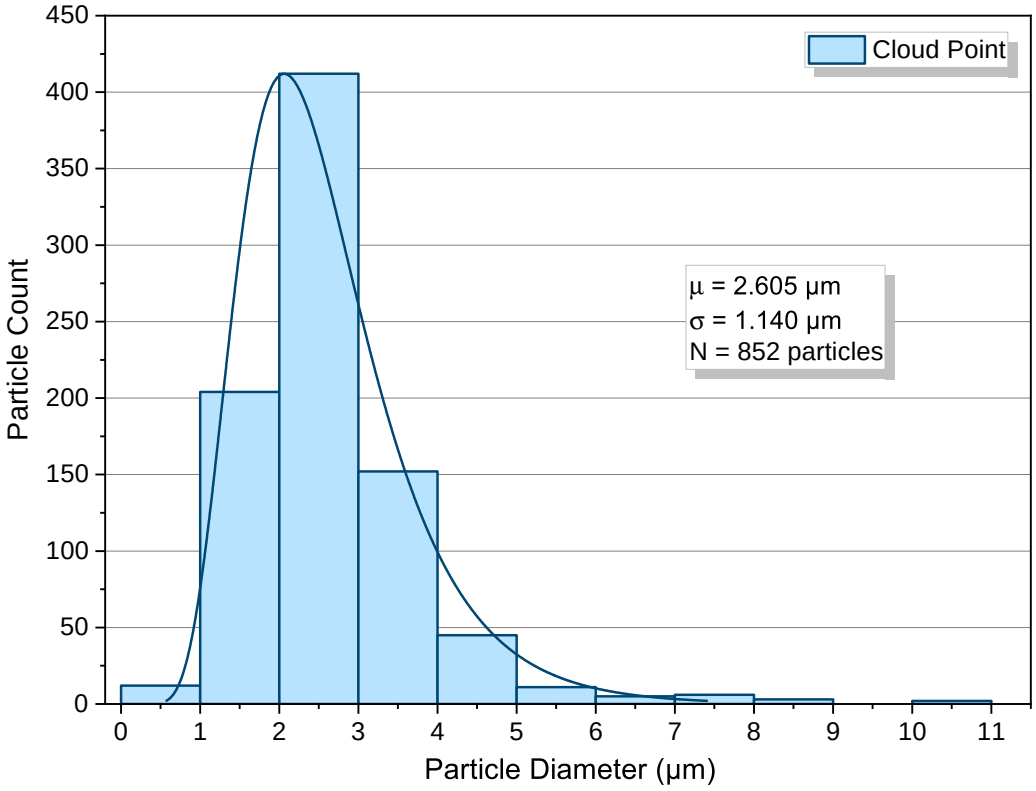

Figure 9. PSD at the cloud point (40.0 °C, 12.37 MPa), following a lognormal distribution (solid blue line): $\mu = 2.605$ µm, $\sigma = 1.140$ µm, $N = 852$, and CV ≈ 0.44; histogram mode ≈ 2.00 µm.

Relative to the one-phase deposition, the mean diameter increased by $\sim 1.47 \times$ (2.605/1.767), and the overall particle morphology evolved from islands to spheres, indicating a transition from heterogeneous surface nucleation and two-dimensional lateral growth to homogeneous nucleation and three-dimensional growth and agglomeration during the 30 min deposition period. Mechanistically, the cloud point lowers the free-energy barrier ΔG^* and critical radius r^* enough for bulk nuclei to appear (accounting for the macroscopic haze in Figure 5B).

3.4. Two-Phase Region

At 40.0 °C and 8.96 MPa, the ternary mixture resides in the two-phase region (see Figure 5C). Under these conditions solvency is poor and both the critical radius r^* and the nucleation barrier ΔG^* are further reduced in comparison to the cloud-point condition. Therefore, during the 30 min deposition period, particle formation is dominated by homogeneous nucleation and rapid growth in solution, followed by surface deposition. Because of the rapid formation of the solid polymer phase, solvent can become trapped inside the polymer particles. During the subsequent depressurization step, the trapped CO_2 and toluene near the particle surface can escape, forming the crater-like voids observed in the SEM micrograph in Figure 10. This figure shows abundant spherical particles with sizes ranging from submicron to over 10 µm, often displaying surface craters. Particle agglomeration is noticeably reduced in comparison to the cloud-point deposition, as agglomeration was likely replaced by coalescence, resulting in the very large particles seen in the figure.

Figure 11 is a histogram illustrating the PSD for deposition in the two-phase region. The PSD is broad and strongly right-skewed, and it follows a lognormal distribution. The upper tail extends to $\sim$30 µm, and the arithmetic descriptors are $\mu = 2.863$ µm and

$\sigma = 2.912$ µm for $N = 1087$ (CV ≈ 1.02). Sampling precision remains adequate for cross-condition comparisons (standard error $\sigma/\sqrt{N} \approx 0.088$ µm; 95% CI $\mu \pm 0.173$ µm). The extreme right tail in Figure 10 suggests particle coalescence in solution prior to and during deposition.

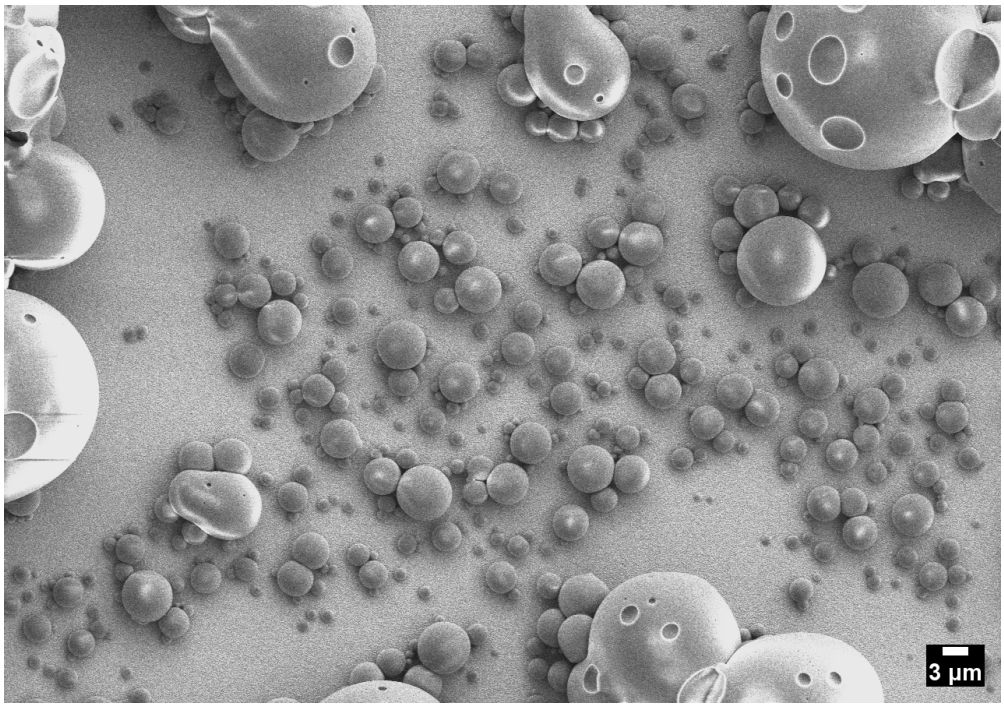

Figure 10. SEM image of the two-phase region (40.0 °C, 8.96 MPa) showing a hierarchical particle population on FTO: numerous small spheres alongside large hollow or pitted poly(TFEMA) particles.

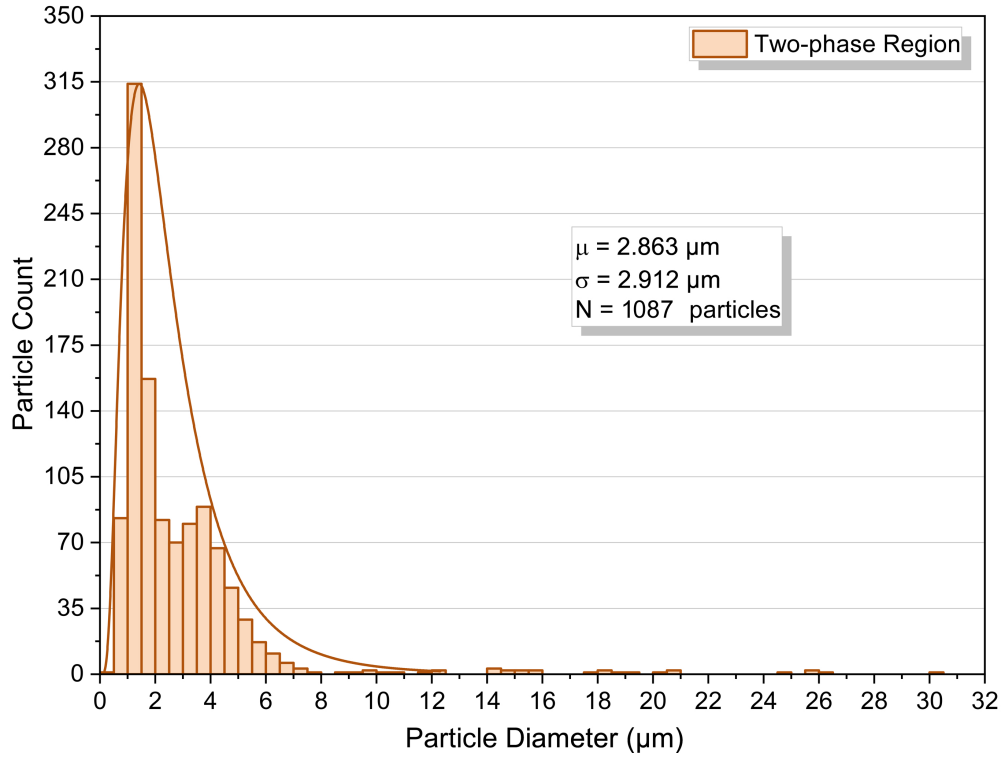

Figure 11. PSD in the two-phase region (40.0 °C, 8.96 MPa), well described by a lognormal fit (solid orange line); broad, right-skewed with a heavy upper tail to ~30 µm. $\mu = 2.863$ µm, $\sigma = 2.912$ µm, $N = 1087$, and CV ≈ 1.02.

Origin of Crater-like Pits (Outgassing Mechanism)

The craters observed on the largest particles arise from outgassing during cooling and depressurization. As the external pressure is lowered, a positive pressure differential is created between the trapped solvent regions within the polymer particles and the surface. When the pressure differential exceeds the stress necessary to overcome the viscoelastic polymer barrier, local rupture vents the pocket, leaving an open crater. Solvent regions trapped deep within the bulk of the larger particles may remain trapped or outgas slowly over time rather than vent through surface rupture.

3.5. Quantitative Cross-Condition Comparison and Mechanistic Synthesis

Figure 12 shows the particle-diameter range for each of the pressure regions. A logarithmic scale was used to help visualize the comparison since the PSDs varied significantly across the three different regions. Three quantitative patterns emerge. First, the mean diameter increases monotonically as the pressure decreases at a fixed temperature, rising from 1.767 μm to 2.605 μm to 2.863 μm for the one-phase, cloud-point, and two-phase conditions, respectively. Second, particle dispersion is non-monotonic as follows: it narrows slightly at the cloud point relative to the one-phase region (CV ≈ 0.44 vs. 0.47) and then broadens sharply in the two-phase region (CV ≈ 1.02). We attribute the modest narrowing at the cloud point to a change in the primary nucleation mechanism, from heterogeneous surface nucleation to the onset of homogeneous bulk nucleation. Third, the two-phase distribution shows a clear separation between the mean and the median together with numerous large-diameter outliers, consistent with the emergence of particle coalescence.

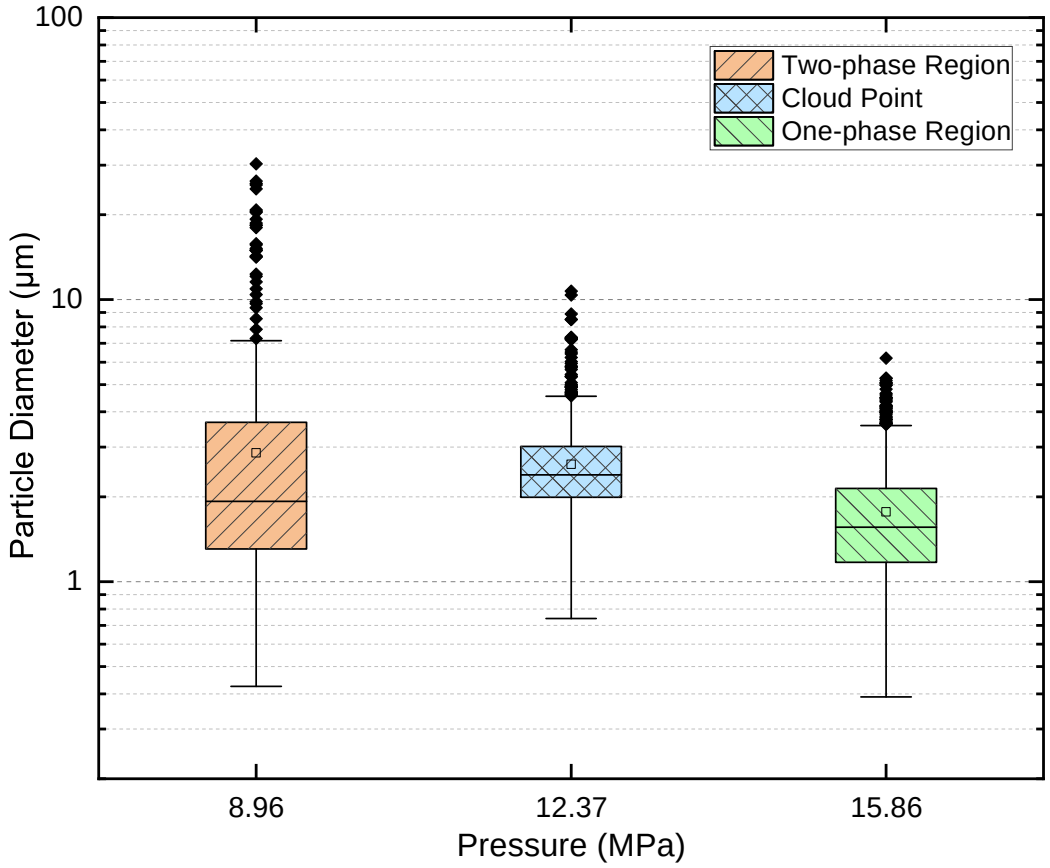

Figure 12. Log-scaled boxplots of poly(TFEMA) particle diameters at 40.0 °C in the one-phase (15.86 MPa), cloud-point (12.37 MPa), and two-phase (8.96 MPa) regions. Boxes show the interquartile range (IQR) with the median as a solid line; squares indicate the mean; whiskers extend to 1.5× IQR; and diamonds denote outliers.

The statistical contrasts in the boxplots align with the regime-specific behavior established earlier. In the one-phase region, bulk nucleation and growth is absent, and the PSD is determined by heterogeneous nucleation at the surface. We also note that the surface-nucleated particles appear as flat, two-dimensional islands rather than spherical particles. Therefore, the PSD would be shifted lower in comparison to the other two regions if mass instead of diameter were used for the comparison. At the cloud point, bulk homogeneous nucleation dominates and is responsible for the observed clustered spheres with limited coalescence. In the two-phase region, nucleation is predominantly homogeneous and rapid, generating a dense population of primary droplets that coalesce in solution, trapping solvent and resulting in a much larger upper range of particle diameters. During depressurization, the outgassing of dissolved CO_2 and toluene produces the observed craters in the larger particles.

The pressure dependence is consistent with classical nucleation ideas as follows: decreasing pressure at fixed temperature raises supersaturation, lowers the free-energy barrier and critical radius, and accelerates nucleation. Surface nucleation maintains a strong heterogeneous contribution at higher pressures, while deep two-phase deposition adds a more substantial homogeneous component. Post-nucleation mass transfer then amplifies dispersion, and the final vent step imprints gas-release signatures on the largest particles. Together, these effects account for the systematic rise in mean size, the slight tightening at the cloud point, and the subsequent broadening with a heavy upper tail.

Sampling precision supports cross-condition inference. The 95% confidence intervals for the mean diameters are $\mu \pm 0.048$ μm for the one-phase condition with $N = 1177$, $\mu \pm 0.077$ μm for the cloud point with $N = 852$, and $\mu \pm 0.173$ μm for the two-phase condition with $N = 1087$.

From a particle-design perspective, we deduce the following:

- One-phase operation favors compact, relatively uniform deposits with minimal interparticle interaction.
- Cloud-point operation increases coverage and shifts sizes upward while retaining a single mode and only modest dispersion.
- Two-phase operation yields the broadest dispersions and the largest outliers as a result of coalescence and vent-induced hollowing.

4. Conclusions

Poly(TFEMA) particle nucleation, growth, and surface deposition were studied in the one-phase, cloud-point, and two-phase regimes from a solution of fixed composition (20 wt% toluene + 1 wt% poly(TFEMA) + 79 wt% scCO_2) at 313.2 K. One-phase deposition yielded sparse, compact surface islands indicative of heterogeneous nucleation and lateral growth along the edges of the nucleated surface islands; cloud-point deposition showed the emergence of homogeneous nucleation in solution with spherical particles and agglomeration; and two-phase deposition produced rapid homogeneous nucleation and particle coalescence, revealing very large particles with surface craters indicative of solvent rupture sites during venting. Fluoropolymers are used in many applications, and the ability to tailor particle nucleation and growth using thermodynamic phase control to alter solvation could provide a useful processing tool for particle design. The experimental results presented here could help guide a comprehensive theoretical nucleation model for this system, but that is beyond the scope of the current investigation.

Author Contributions: Conceptualization, J.R.Z. and G.C.T.; methodology, J.R.Z. and G.C.T.; investigation, J.R.Z.; formal analysis, J.R.Z. and G.C.T.; writing—original draft preparation, J.R.Z.; writing—review and editing, J.R.Z. and G.C.T.; supervision, G.C.T. All authors have read and agreed to the published version of the manuscript.

Funding: This research received no external funding.

Institutional Review Board Statement: Not applicable.

Informed Consent Statement: Not applicable.

Data Availability Statement: Data supporting the findings of this study are available from the corresponding author upon reasonable request.

Acknowledgments: The authors gratefully acknowledge the Nanomaterials Characterization Center at Virginia Commonwealth University for granting access to sputter coating, plasma cleaning, and SEM facilities. The authors thank Carl Mayer (NCC Scientist) and Dmitry Pestov (Senior NCC Scientist) for providing training and technical guidance in sputter coating, plasma cleaning, and SEM operation.

Conflicts of Interest: The authors declare no conflicts of interest.

Abbreviations

AG–HGK	Altunin–Gadetskii–Haar–Gallagher–Kell (equation of state for CO_2)
CCD	Charge-coupled device (camera)
CV	Coefficient of variation (σ/μ)
DI	Deionized (water)
EOS	Equation of state
FTO	Fluorine-doped tin oxide
IPA	Isopropyl alcohol
IQR	Interquartile range
PDI	Polydispersity index
PSD	Particle-size distribution
PTFE	Polytetrafluoroethylene
$scCO_2$	Supercritical carbon dioxide
SEM	Scanning electron microscopy
TFEMA	2,2,2-trifluoroethyl methacrylate (poly(TFEMA) denotes the homopolymer)
T_g	Glass transition temperature

Nomenclature

Symbol	Description	Units
P	Pressure	MPa
T	Temperature	K (or °C)
ρ_{scCO_2}	Supercritical CO_2 density (EOS)	kg m^{-3}
m_{scCO_2}	Mass of $scCO_2$ charged	g
m_{Tol}	Mass of toluene charged	g
V_{Tol}	Volume of toluene charged	mL
m_{Poly}	Mass of poly(TFEMA)	g
w_p	Polymer mass fraction	wt%
P_{cp}	Cloud-point pressure	MPa
N	Sample size (particle count)	–
μ	Mean particle diameter	μm
σ	Standard deviation of diameter	μm
CV	Coefficient of variation (σ/μ)	–
r^*	Critical nucleus radius	nm (or m)
ΔG^*	Nucleation free-energy barrier	J

References

1. Ovaskainen, L.; Rodriguez-Meizoso, I.; Birkin, N.A.; Howdle, S.M.; Gedde, U.; Wågberg, L.; Turner, C. Towards superhydrophobic coatings made by non-fluorinated polymers sprayed from a supercritical solution. *J. Supercrit. Fluids* **2013**, *77*, 134–141. [CrossRef]
2. Vasylyshyn, T.; Patsula, V.; Filipová, M.; Konefal, R.L.; Horák, D. Poly(glycerol monomethacrylate)-encapsulated upconverting nanoparticles prepared by miniemulsion polymerization: Morphology, chemical stability, antifouling properties and toxicity evaluation. *Nanoscale Adv.* **2023**, *5*, 6979–6989. [CrossRef]
3. Lv, C.; Liao, X.; Zou, F.; Tang, W.; Xing, S.; Li, G. Generating porous polymer microspheres with cellular surface via a gas-diffusion confined $scCO_2$ foaming technology to endow the super-hydrophobic coating with hierarchical roughness. *Chem. Eng. J.* **2022**, *442*, 136192. [CrossRef]
4. Zhu, H.; Wang, W.; Wang, Y.; Lin, Z.; Ji, H.; Chen, X.; Li, G.; Ma, Y.; Xie, L. Preparation of PP/PC Light-Diffusing Materials with UV-Shielding Property. *Polym. Compos.* **2023**, *44*, 5553–5566. [CrossRef]
5. Zhang, A.; Zhang, Q.; Bai, H.; Li, L.; Li, J. Polymeric nanoporous materials fabricated with supercritical CO_2 and CO_2-expanded liquids. *Chem. Soc. Rev.* **2014**, *43*, 6938–6953. [CrossRef] [PubMed]
6. Barroso, T.; Temtem, M.; Casimiro, T.; Aguiar-Ricardo, A. Development of pH-responsive poly(methylmethacrylate-co-methacrylic acid) membranes using $scCO_2$ technology. Application to protein permeation. *J. Supercrit. Fluids* **2009**, *51*, 57–66. [CrossRef]
7. Scholes, C.A.; Kanehashi, S. Polymeric membrane gas separation performance improvements through supercritical CO_2 treatment. *J. Membr. Sci.* **2018**, *566*, 239–248. [CrossRef]
8. Ratcharak, O.; Sane, A. Surface coating with poly(trifluoroethyl methacrylate) through rapid expansion of supercritical CO_2 solutions. *J. Supercrit. Fluids* **2014**, *89*, 106–112. [CrossRef]
9. Leitner, W. Designed to dissolve. *Nature* **2000**, *405*, 129–130. [CrossRef]
10. Zhang, X.; Heinonen, S.; Levänen, E. Applications of supercritical carbon dioxide in materials processing and synthesis. *RSC Adv.* **2014**, *4*, 61137–61152. [CrossRef]
11. Tomasko, D.L.; Li, H.; Liu, D.; Han, X.; Wingert, M.J.; Lee, L.J.; Koelling, K.W. A Review of CO_2 Applications in the Processing of Polymers. *Ind. Eng. Chem. Res.* **2003**, *42*, 6431–6456. [CrossRef]
12. Tutek, K.; Masek, A.; Kosmalska, A.; Cichosz, S. Application of Fluids in Supercritical Conditions in the Polymer Industry. *Polymers* **2021**, *13*, 729. [CrossRef] [PubMed]
13. Kortsen, K.; Fowler, H.R.; Jacob, P.L.; Krumins, E.; Lentz, J.C.; Souhil, M.R.; Taresco, V.; Howdle, S.M. Exploiting the tuneable density of $scCO_2$ to improve particle size control for dispersion polymerisations in the presence of poly(dimethyl siloxane) stabilisers. *Eur. Polym. J.* **2022**, *168*, 111108. [CrossRef]
14. Hakuta, Y.; Hayashi, H.; Arai, K. Fine particle formation using supercritical fluids. *Curr. Opin. Solid State Mater. Sci.* **2003**, *7*, 341–351. [CrossRef]
15. Yan, H.; Sato, T.; Komago, D.; Yamaguchi, A.; Oyaizu, K.; Yuasa, M.; Otake, K. Electrochemical Synthesis of a Polypyrrole Thin Film with Supercritical Carbon Dioxide as a Solvent. *Langmuir* **2005**, *21*, 12303–12308. [CrossRef]
16. Medina-Gonzalez, Y.; Camy, S.; Condoret, J.S. $scCO_2$/Green Solvents: Biphasic Promising Systems for Cleaner Chemicals Manufacturing. *ACS Sustain. Chem. Eng.* **2014**, *2*, 2623–2636. [CrossRef]
17. Wood, C.D.; Tan, B.; Zhang, H.; Cooper, A.I. Chapter 21—Supercritical Carbon Dioxide as a Green Solvent for Polymer Synthesis. In *Thermodynamics, Solubility and Environmental Issues*; Letcher, T.M., Ed.; Elsevier: Amsterdam, The Netherlands, 2007; pp. 383–396. [CrossRef]
18. Khanyile, A.; Andrew, J.; Paul, V.; Sithole, B. A comparative study of supercritical fluid extraction and accelerated solvent extraction of lipophilic compounds from lignocellulosic biomass. *Sustain. Chem. Pharm.* **2022**, *26*, 100608. [CrossRef]
19. do Espirito Santo, A.T.; Siqueira, L.M.; Almeida, R.N.; Vargas, R.M.F.; do N Franceschini, G.; Kunde, M.A.; Cappellari, A.R.; Morrone, F.B.; Cassel, E. Decaffeination of yerba mate by supercritical fluid extraction: Improvement, mathematical modelling and infusion analysis. *J. Supercrit. Fluids* **2021**, *168*, 105096. [CrossRef]
20. Marco, I.D.; Riemma, S.; Iannone, R. Supercritical Carbon Dioxide Decaffeination Process: A Life Cycle Assessment Study. *Chem. Eng. Trans.* **2017**, *57*, 1699–1704. [CrossRef]
21. Zhang, H.; Huang, T.; Liao, X.; Zhou, Y.; Chen, S.; Chen, J.; Xiong, W. Extraction of Camphor Tree Essential Oil by Steam Distillation and Supercritical CO_2 Extraction. *Molecules* **2022**, *27*, 5385. [CrossRef]
22. Yıldırım, M.; Erşatır, M.; Poyraz, S.; Amangeldinova, M.; Kudrina, N.O.; Terletskaya, N.V. Green Extraction of Plant Materials Using Supercritical CO_2: Insights into Methods, Analysis, and Bioactivity. *Plants* **2024**, *13*, 2295. [CrossRef] [PubMed]
23. Handy, K.; Tepper, G.C. Incorporation of Poly(TFEMA) in Perovskite Thin Films Using a Supercritical Fluid. *Molecules* **2023**, *28*, 5385. [CrossRef]
24. von Schnitzler, J.; Eggers, R. Mass transfer in polymers in a supercritical CO_2-atmosphere. *J. Supercrit. Fluids* **1999**, *16*, 81–92. [CrossRef]

25. Furtado, A.I.; Bonifácio, V.D.B.; Viveiros, R.; Casimiro, T. Design of Molecularly Imprinted Polymers Using Supercritical Carbon Dioxide Technology. *Molecules* **2024**, *29*, 926. [CrossRef]
26. Naguib, H.E.; Park, C.B.; Song, S.W. Effect of Supercritical Gas on Crystallization of Linear and Branched Polypropylene Resins with Foaming Additives. *Ind. Eng. Chem. Res.* **2005**, *44*, 6685–6691. [CrossRef]
27. Luna-Bárcenas, G.; Mawson, S.; Takishima, S.; DeSimone, J.M.; Sanchez, I.C.; Johnston, K.P. Phase behavior of poly(1,1-dihydroperfluorooctylacrylate) in supercritical carbon dioxide. *Fluid Phase Equilibria* **1998**, *146*, 325–337. [CrossRef]
28. Blackburn, J.M.; Long, D.P.; Cabañas, A.; Watkins, J.J. Deposition of Conformal Copper and Nickel Films from Supercritical Carbon Dioxide. *Science* **2001**, *294*, 141–145. [CrossRef]
29. Cabañas, A.; Long, D.P.; Watkins, J.J. Deposition of Gold Films and Nanostructures from Supercritical Carbon Dioxide. *Chem. Mater.* **2004**, *16*, 2028–2033. [CrossRef]
30. Rasadujjaman, M.; Watanabe, M.; Kondoh, E. Codeposition of Cu/Ni thin films from mixed precursors in supercritical carbon dioxide solutions. *Jpn. J. Appl. Phys.* **2014**, *53*, 5–7. [CrossRef]
31. Pandiyarajan, S.; Hsiao, P.J.; Liao, A.H.; Ganesan, M.; Manickaraj, S.S.M.; Lee, C.T.; Huang, S.T.; Chuang, H.C. Influence of ultrasonic combined supercritical-CO_2 electrodeposition process on copper film fabrication: Electrochemical evaluation. *Ultrason. Sonochemistry* **2021**, *74*, 105555. [CrossRef] [PubMed]
32. Ganesan, M.; Liu, C.C.; Pandiyarajan, S.; Lee, C.T.; Chuang, H.C. Post-supercritical CO_2 electrodeposition approach for Ni-Cu alloy fabrication: An innovative eco-friendly strategy for high-performance corrosion resistance with durability. *Appl. Surf. Sci.* **2022**, *577*, 151955. [CrossRef]
33. Hosokawa, S.; Tomita, E.; Kanehashi, S.; Ogino, K. Study on effect of supercritical CO_2 on structural ordering and charge transporting property in thiophene-based block copolymer. *Jpn. J. Appl. Phys.* **2022**, *61*, 021001. [CrossRef]
34. Sajfrtová, M.; Cerhová, M.; Jandová, V.; Dřínek, V.; Daniš, S.; Matějová, L. The effect of type and concentration of modifier in supercritical carbon dioxide on crystallization of nanocrystalline titania thin films. *J. Supercrit. Fluids* **2018**, *133*, 211–217. [CrossRef]
35. Wei, M.; Wang, K.; Yanagida, M.; Sugihara, H.; Morris, M.A.; Holmes, J.D.; Zhou, H. Supercritical fluid processing of mesoporous crystalline TiO_2 thin films for highly efficient dye-sensitized solar cells. *J. Mater. Chem.* **2007**, *17*, 3888–3893. [CrossRef]
36. Sanli, D.; Bozbag, S.E.; Erkey, C. Synthesis of nanostructured materials using supercritical CO_2: Part I. Physical transformations. *J. Mater. Sci.* **2012**, *47*, 2995–3025. [CrossRef]
37. Kaleva, A.; Heinonen, S.; Nikkanen, J.P.; Levänen, E. Synthesis and Crystallization of Titanium Dioxide in Supercritical Carbon Dioxide ($scCO_2$). *IOP Conf. Ser. Mater. Sci. Eng.* **2017**, *175*, 012034. [CrossRef]
38. Wei, T.Y.; Chen, C.H.; Chien, H.C.; Lu, S.Y.; Hu, C.C. A Cost-Effective Supercapacitor Material of Ultrahigh Specific Capacitances: Spinel Nickel Cobaltite Aerogels from an Epoxide-Driven Sol-Gel Process. *Adv. Mater.* **2010**, *22*, 347–351. [CrossRef] [PubMed]
39. Pu, N.W.; Wang, C.A.; Sung, Y.; Liu, Y.M.; Ger, M.D. Production of few-layer graphene by supercritical CO_2 exfoliation of graphite. *Mater. Lett.* **2009**, *63*, 1987–1989. [CrossRef]
40. Wang, Y.; Zhou, C.; Wang, W.; Zhao, Y. Preparation of Two Dimensional Atomic Crystals-BN, WS_2 and MoS_2 by Supercritical CO_2 Assisted with Ultrasonic. *Ind. Eng. Chem. Res.* **2013**, *52*, 4379–4382. [CrossRef]
41. Rindfleisch, F.; DiNoia, T.P.; McHugh, M.A. Solubility of Polymers and Copolymers in Supercritical CO_2. *J. Phys. Chem.* **1996**, *100*, 15581–15587. [CrossRef]
42. Ekart, M.P.; Bennett, K.L.; Ekart, S.M.; Gurdial, G.S.; Liotta, C.L.; Eckert, C.A. Cosolvent Interactions in Supercritical Fluid Solutions. *AIChE J.* **1993**, *39*, 235–248. [CrossRef]
43. Beckman, E.J. Supercritical and near-critical CO_2 in green chemical synthesis and processing. *J. Supercrit. Fluids* **2004**, *28*, 121–191. [CrossRef]
44. Ting, Y.S.; Hsieh, C.M. Prediction of solid solute solubility in supercritical carbon dioxide with organic cosolvents from the PR+COSMOSAC equation of state. *Fluid Phase Equilibria* **2017**, *431*, 48–57. [CrossRef]
45. Ren, H.; Song, J.; Xu, Q.; Yin, J. Solubility of the silver nitrate in supercritical carbon dioxide with ethanol and ethylene glycol as double cosolvents: Experimental determination and correlation. *Chin. J. Chem. Eng.* **2019**, *27*, 400–404. [CrossRef]
46. Gurina, D.L.; Antipova, M.L.; Odintsova, E.G.; Petrenko, V.E. The study of peculiarities of parabens solvation in methanol- and acetone-modified supercritical carbon dioxide by computer simulation. *J. Supercrit. Fluids* **2017**, *126*, 47–54. [CrossRef]
47. Tomasko, D.L.; Knutson, B.L.; Pouillot, F.; Liotta, C.L.; Eckert, C.A. Spectroscopic study of structure and interactions in cosolvent-modified supercritical fluids. *J. Phys. Chem.* **1993**, *97*, 11823–11834. [CrossRef]
48. Yang, H.; Zhong, C. Modeling of the solubility of aromatic compounds in supercritical carbon dioxide–cosolvent systems using SAFT equation of state. *J. Supercrit. Fluids* **2005**, *33*, 99–106. [CrossRef]
49. Zhang, G.; Wu, T.; Li, J.; Pang, Q.; Yang, H.; Liu, G.; Huang, H.; Zhu, Y. Dynamics Simulation of the Effect of Cosolvent on the Solubility and Tackifying Behavior of PDMS Tackifier in Supercritical CO_2 Fracturing Fluid. *Colloids Surf. A Physicochem. Eng. Asp.* **2023**, *662*, 130985. [CrossRef]

50. Zhang, H.; Liu, Z.; Han, B. Critical points and phase behavior of toluene-CO_2 and toluene-H_2-CO_2 mixture in CO2-rich region. *J. Supercrit. Fluids* **2000**, *18*, 185–192. [CrossRef]
51. Matsukawa, H.; Tsuji, T.; Otake, K. Measurement of the Density of Carbon Dioxide/Toluene Homogeneous Mixtures and Correlation with Equations of State. *J. Chem. Thermodyn.* **2022**, *164*, 106618. [CrossRef]
52. Wu, J.; Pan, Q.; Rempel, G.L. Pressure-Density-Temperature Behavior of CO_2/Acetone, CO_2/Toluene, and CO_2/Monochlorobenzene Mixtures in the Near-Critical Region. *J. Chem. Eng. Data* **2004**, *49*, 976–979. [CrossRef]
53. Rowane, A.J.; Mallepally, R.R.; Bamgbade, B.A.; Newkirk, M.S.; Baled, H.O.; Burgess, W.A.; Gamwo, I.K.; Tapriyal, D.; Enick, R.M.; McHugh, M.A. High-temperature, high-pressure viscosities and densities of toluene. *J. Chem. Thermodyn.* **2017**, *115*, 34–46. [CrossRef]
54. Pitzer, K.S.; Schreiber, D.R. Improving equation-of-state accuracy in the critical region; equations for carbon dioxide and neopentane as examples. *Fluid Phase Equilibria* **1988**, *41*, 1–17. [CrossRef]
55. Ameduri, B. Fluoropolymers: The right material for the right applications. *Chem.–Eur. J.* **2018**, *24*, 18830–18841. [CrossRef]
56. Ciardelli, F.; Rubino, G.; Ranieri, G.; Licciulli, A.; Laviano, R. Fluorinated polymeric materials for the protection of monumental buildings. *Macromol. Symp.* **2000**, *152*, 211–222. [CrossRef]
57. Leivo, E.; Wilenius, T.; Kinos, T.; Vuoristo, P.; Mäntylä, T. Properties of thermally sprayed fluoropolymer PVDF, ECTFE, PFA and FEP coatings. *Prog. Org. Coat.* **2004**, *49*, 69–73. [CrossRef]
58. Kwon, S.; Bae, W.; Lee, K.; Byun, H.S.; Kim, H. High Pressure Phase Behavior of Carbon Dioxide + 2,2,2-Trifluoroethyl Methacrylate and + Poly(2,2,2-trifluoroethyl methacrylate) Systems. *J. Chem. Eng. Data* **2007**, *52*, 89–92. [CrossRef]
59. Kwon, S.; Bae, W.; Kim, H. The Effect of CO_2 in Free-radical Polymerization of 2,2,2-Trifluoroethyl Methacrylate. *Korean J. Chem. Eng.* **2004**, *21*, 910–914. [CrossRef]
60. Zelaya, J.R.; Tepper, G.C. Cloud Point Behavior of Poly(trifluoroethyl methacrylate) in Supercritical CO_2–Toluene Mixtures. *Molecules* **2025**, *30*, 1199. [CrossRef]
61. Byun, H.S.; Kim, C.R.; Yoon, S.D. Cloud-point measurement of binary and ternary mixtures for the P(MMA-co-PnFPA) in supercritical fluoric solvents. *J. Supercrit. Fluids* **2017**, *120*, 226–239. [CrossRef]
62. Xu, A.; Zhang, L.; Ma, J.; Ma, Y.; Geng, B.; Zhang, S. Preparation and surface properties of poly(2,2,2-trifluoroethyl methacrylate) coatings modified with methyl acrylate. *J. Coat. Technol. Res.* **2016**, *13*, 795–804. [CrossRef]
63. Annohene, G.; Tepper, G. Moisture Stability of Perovskite Solar Cells Processed in Supercritical Carbon Dioxide. *Molecules* **2021**, *26*, 7570. [CrossRef]
64. Annohene, G.; Tepper, G.C. Efficient perovskite solar cells processed in supercritical carbon dioxide. *J. Supercrit. Fluids* **2021**, *171*, 105203. [CrossRef]
65. Annohene, G.; Pascucci, J.; Pestov, D.; Tepper, G.C. Supercritical fluid-assisted crystallization of $CH_3NH_3PbI_3$ perovskite films. *J. Supercrit. Fluids* **2020**, *156*, 104684. [CrossRef]
66. Annohene, G.; Tepper, G.C. Low temperature formation of $CH_3NH_3PbI_3$ perovskite films in supercritical carbon dioxide. *J. Supercrit. Fluids* **2019**, *154*, 104604. [CrossRef]
67. Schmelzer, J.; Röpke, G.; Priezzhev, V.B. *Nucleation Theory and Applications*; Wiley Online Library: Hoboken, NJ, USA, 2005; Volume 76, p. 472. [CrossRef]
68. Oxtoby, D.W. Homogeneous nucleation: Theory and experiment. *J. Phys. Condens. Matter* **1992**, *4*, 7627. [CrossRef]
69. Kalikmanov, V.I. Classical Nucleation Theory. In *Nucleation Theory*; Springer: Dordrecht, The Netherlands, 2013; pp. 17–41. [CrossRef]
70. Kashchiev, D. *Nucleation*; Elsevier: Amsterdam, The Netherlands, 2000.
71. Kalikmanov, V.I. Heterogeneous Nucleation. In *Nucleation Theory*; Springer: Dordrecht, The Netherlands, 2013; pp. 253–276. [CrossRef]
72. Liu, X. Heterogeneous nucleation or homogeneous nucleation? *J. Chem. Phys.* **2000**, *112*, 9949–9955. [CrossRef]
73. Lifshitz, I.M.; Slyozov, V.V. The kinetics of precipitation from supersaturated solid solutions. *J. Phys. Chem. Solids* **1961**, *19*, 35–50. [CrossRef]

Disclaimer/Publisher's Note: The statements, opinions and data contained in all publications are solely those of the individual author(s) and contributor(s) and not of MDPI and/or the editor(s). MDPI and/or the editor(s) disclaim responsibility for any injury to people or property resulting from any ideas, methods, instructions or products referred to in the content.